



RuO₂–SiO₂ mixed oxides as corrosion-resistant catalyst supports for polymer electrolyte fuel cells

Amod Kumar, Vijay K. Ramani*

Center for Electrochemical Science and Engineering, Department of Chemical & Biological Engineering, 10 W 33rd Street, 127 Perlstein Hall, Illinois Institute of Technology, Chicago, IL 60616, USA

ARTICLE INFO

Article history:

Received 21 September 2012

Received in revised form 23 January 2013

Accepted 1 February 2013

Available online 14 February 2013

Keywords:

Electrocatalyst support

Polymer electrolyte fuel cell

Carbon corrosion

Mixed metal oxides

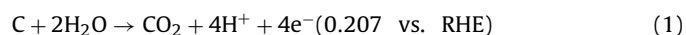
ABSTRACT

The objective of this study was to evaluate the suitability of mixed oxides of silica (SiO₂) and ruthenia (RuO₂) for use as electrocatalyst supports in polymer electrolyte fuel cells (PEFCs). The RuO₂:SiO₂ oxides were synthesized in three different molar ratios (0.1:0.9, 0.3:0.7 and 0.5:0.5). Of these formulations, RuO₂–SiO₂ (0.5:0.5) displayed high BET surface area (~290 m² g^{−1}), high electronic conductivity (>5 S cm^{−1}), and outstanding electrochemical stability (change in double layer capacitance of <10% compared to 360% for Vulcan XC72 carbon upon rigorous accelerated potential cycling tests that mimic automotive drive cycles). The RuO₂–SiO₂ (0.5:0.5) support material was subsequently catalyzed by deposition of 24 wt% of platinum nanoparticles. The resultant electrocatalyst yielded a mass activity of 50 mA mg_{Pt}^{−1} and an area specific activity of 156.3 μA cm^{−2} at 0.9 V vs. RHE when tested in a fuel cell operating at 80 °C and 75% relative humidity.

© 2013 Elsevier B.V. All rights reserved.

1. Introduction

The modular nature of polymer electrolyte fuel cells (PEFCs) renders them suitable for applications in the automotive, stationary, and portable power/military sectors. Two major issues currently precluding wide-scale commercialization of PEFCs are component cost and durability. From the perspective of component durability, the current state-of-the-art electrocatalyst, viz. platinum (Pt) supported on high surface area carbon, suffers substantial degradation during fuel cell operation. Multiple degradation mechanisms have been recognized; mechanisms specific to the active catalyst particle include platinum dissolution/migration, sintering and agglomeration [1]. Another key pathway for electrocatalyst degradation is the corrosion of the carbon support. Carbon is readily oxidized to carbon dioxide under certain operating conditions. Carbon corrosion occurs via the following reaction [2]:



While this reaction is always thermodynamically favorable at the PEFC cathode during operation, the reaction kinetics, fortuitously, are rather poor. However, the rate constant for the carbon corrosion reaction is considerably enhanced due to the mixed reactant fronts and resultant spikes in cathode potential that arise during stack start-up and shut-down (unavoidable in automotive applications), leading to significantly accelerated corrosion rates at

the cathode. If fuel starvation occurs due to overutilization of fuel or due lack of access of fuel to catalyst site, the anode also suffers from carbon corrosion, wherein carbon is sacrificially oxidized in place of the fuel [3,4]. The carbon corrosion process leads to electrically isolated Pt particles that are separated from the support material and also contributes to platinum agglomeration and a concomitant drop in platinum utilization. The catalyst mass activity and fuel cell performance are consequently reduced, leading to lower stack lifetime.

Carbon is an attractive choice for PEFC electrocatalyst support due to its high electron conductivity, high stability in acid media under normal operating conditions, and high surface area that permits excellent dispersion of the active electrocatalyst [5–7]. The key drawback is its propensity to corrosion, as discussed earlier. Any viable alternate (non-carbon) catalyst support must possess all the above properties in addition to being corrosion-resistant during excursions in electrode potential that occur during PEFC start-stop and fuel starvation.

A wide range of non-carbon supports have been examined for use in fuel cell application [8]. Transition metal nitrides such as TiN exhibit high electronic conductivity and are extremely robust and corrosion-resistant [9]. While some studies have reported good electrocatalyst activity with TiN as a support [10,11], its long-term stability in acidic medium is not very high and hence TiN is not suitable for fuel cells [12] that operate in acidic media. Transition metal carbides exhibit high conductivity and stability and are a viable alternative support material. Tungsten carbide supported platinum has been previously shown to have good catalytic activity [13–15]. This material, however, suffers from low surface area and requires

* Corresponding author. Tel.: +1 312 567 3064; fax: +1 312 567 8874.
E-mail address: ramani@iit.edu (V.K. Ramani).

modification to exhibit higher surface area and permit high dispersion of platinum electrocatalyst [16–18]. Other carbides with promising characteristics are boron carbide (B_4C), titanium carbide (TiC) and silicon carbide (SiC) [8].

Several studies have examined the use of conducting metal oxides as the electrocatalyst support material in PEFCs. These oxides have been shown to possess high electron conductivities, thermal and mechanical strength, and reasonable surface area. Magneli phase titania (Ti_4O_7) having very high electron conductivity of $\sim 1000\text{ S cm}^{-1}$ has been synthesized [19,20] and shown to have high catalytic activity and stability in an operating fuel cell; however its surface area is quite low [20–22]. Titanium dioxide (TiO_2) is known to possess high stability and is reported to exhibit synergistic metal-support interactions with platinum, resulting in an improved catalytic activity compared to a commercial carbon supported platinum electrocatalyst [23]. However, due to its low electron conductivity, TiO_2 is typically doped with metals such as ruthenium and niobium. Platinum supported on niobium, tungsten doped TiO_2 has been synthesized and shown to have exhibit high activity for the oxygen reduction reaction [24,25]. Similarly, platinum supported on ruthenium doped TiO_2 has also been shown to exhibit high electrochemical performance and good stability [26,27]. There are other metal oxides that have been used as non-carbon supports. Tin oxide (SnO_2) [28] showed high activity for the oxygen reduction reaction, however no stability tests were reported using this material. Tungsten oxide (WO_x) [29–31] has been studied, although tungsten dissolution in acid media is a concern. Sulfated zirconium oxide ($S\text{-}ZrO_2$) [32,33] has been postulated as an attractive option because of its added proton conductivity, however its electron conductivity is low. Indium tin oxide (ITO) [34] has been shown to possess high electron conductivity and stability but has lower activity than Pt/C, likely due to its lower surface area leading to poor platinum dispersion.

Silica (SiO_2) has been used as a support material for catalysts used in reactions such as the production of hydrogen from methanol by partial oxidation, and steam reforming, where calcined SBA-15 has been used as a support for Pd–Zn catalysts [35]. Silica is an attractive candidate for use as a catalyst support because of its extremely high surface area and uniform pore distribution [36]. Platinum particles with a narrow size distribution have been dispersed uniformly in a silica matrix and shown to have high catalytic activity for CO oxidation [37]. Likewise, ruthenium oxide (RuO_2) has been widely used in electrochemical capacitors [38,39], electrolyzers [40], and even in fuel cells, wherein Pt supported on the hydrated form of RuO_2 has been shown to be an active catalyst for methanol oxidation [41,42].

In this study, high surface area SiO_2 doped with RuO_2 has been investigated to determine its applicability as an alternate, corrosion-resistant electrocatalyst support. The underlying hypothesis tested in this study is that the addition of RuO_2 into the SiO_2 network will yield a corrosion-resistant, high-surface area support with electron conductivity comparable to carbon, and high electrochemical stability that is much superior to carbon.

2. Experimental

A list of reagents used and a schematic describing the evolution of support and electrocatalyst morphology is provided in the supporting information section (Fig. S1).

2.1. Synthesis of RuO_2 – SiO_2

Silica was synthesized using a templating procedure [43]. 11.16 mL of tetraethylorthosilicate (TEOS) was used as a precursor for the silica and 1.82 g of cetyltrimethylammonium bromide

($C_{16}TAB$) was used as a structure directing agent to obtain a mesoporous architecture. 0.56 mL of nitric acid was used as the catalyst for TEOS hydrolysis and condensation. 1.37 mL polyethylene glycol (MW 10,000) was used as the phase-separating agent. The procedure followed was adopted from literature [43]. Ruthenium acetylacetonate ($Ru(acac)_3$) was used as the ruthenium precursor and was dispersed inside the SiO_2 mesostructure using supercritical carbon dioxide ($scCO_2$) as the solvent. Acetone (10 mL) mixed with desired amount of $Ru(acac)_3$ (2.65 g to obtain RuO_2 – SiO_2 (0.5:0.5)) and 0.4 g SiO_2 was placed in a pressure vessel (100 mL volume) and placed inside an oven, in accordance with the method reported in the literature [44]. The pressure vessel was connected to a liquid CO_2 cylinder and was filled with CO_2 at 32 MPa, following which the vessel was heated to 100°C . Under these conditions, CO_2 existed in the supercritical state; the $Ru(acac)_3$ was fully soluble in the supercritical CO_2 . The solubilized precursor was distributed uniformly throughout the pores of the silica framework under supercritical conditions. Following deposition, the deposited $Ru(acac)_3$ was converted to RuO_2 by thermal decomposition, by heating the impregnated silica in a oven at 600°C to yield pure RuO_2 within the silica network. The high decomposition temperature ensured complete conversion of precursor to RuO_2 and helped avoid the formation of metallic ruthenium [45]. It also helped avoid the cumbersome two-step process of reduction of $Ru(acac)_3$ to metallic ruthenium, followed by subsequent oxidation to RuO_2 [46]. The molar ratios of RuO_2 – SiO_2 synthesized in this study were: 0.1:0.9, 0.3:0.7 and 0.5:0.5 respectively. A schematic describing the evolution of the microstructure of the mixed-oxide is shown in Fig. S1.

2.2. Synthesis of Pt/ RuO_2 – SiO_2

A conventional impregnation–reduction procedure [47] was used for the deposition of platinum nanoparticles within the synthesized supports. An aqueous solution of 0.25 g of hexachloroplatinic acid ($H_2PtCl_6\cdot 6H_2O$) was dissolved into a dispersion of 0.3 g RuO_2 – SiO_2 and the resultant mixture was stirred for 2 h. An excess amount of 0.05 M sodium borohydride was then added dropwise under stirring to reduce the platinum precursor to platinum nanoparticles. The resultant catalyzed supports were washed, filtered and dried at room temperature to obtain Pt/ RuO_2 – SiO_2 particles.

2.3. Microstructure characterization

Transmission electron microscopy (TEM) micrographs of the various samples were obtained using a JEOL-3010F electron microscope operating at 300 kV. X-ray powder diffraction patterns were measured on a Bruker D2 Phaser diffractometer equipped with a LynxEye position-sensitive detector. Samples were either mounted in standard sample holders, or as thin layers mounted in zero-background cells using double-sided adhesive tape. The experimental conditions were 20 – $130\ 2\theta$, 0.0202144° steps, 0.5 s/step , 0.6 mm divergence slit, 2.5 E Soller slits, 3 mm scatter screen height. Quantitative phase analysis of the crystalline phases was carried out by the Rietveld method using the General Structure Analysis System (GSAS) [48]. The Brunauer–Emmet–Teller (BET) method was used to calculate specific surface area by nitrogen sorption at -196°C . Inductively coupled plasma mass spectroscopy (ICP-MS) was used to estimate the platinum loading (in wt%) in the support.

2.4. Electronic properties

To determine electron conductivity of the prepared mixed oxides, electrochemical impedance spectroscopy measurements

Table 1
Crystalline phases of RuO₂–SiO₂ catalyst support.

Samples	RuO ₂ –SiO ₂ (0.1:0.9)	RuO ₂ –SiO ₂ (0.3:0.7)	RuO ₂ –SiO ₂ (0.5:0.5)	24% Pt/RuO ₂ –SiO ₂ (0.5:0.5)
RuO ₂ (wt%)	100	99.8(1)	98.3(1)	41.8(1)
<i>a</i> (Å)	4.4986(2)	4.49294(9)	4.49401(6)	4.4936(2)
<i>c</i> (Å)	3.1106(2)	3.105(7)	3.10503(5)	3.1049(1)
Size (Å)	780(30)	2600(150)	1310(20)	1430(80)
Strain (%)	0.44(3)	0.40(1)	0.35(1)	0.44(1)
Pt (wt%)				58.2(1)
<i>a</i> (Å)		n/a		3.9204(2)
Size (Å)				58(1)

were performed on pellet samples using a Gamry potentiostat over the frequency range of 0.1–10⁵ Hz with an oscillating voltage of 10 mV. For sample preparation and other experimental details, please refer to the corresponding sub-section under supporting information.

2.5. Electrochemical properties

All electrochemical measurements were performed in a three-compartment electrochemical cell using 0.1 M HClO₄ as the electrolyte: (i) a glassy carbon disk (0.196 cm²) with a thin layer of the active material deposited on top was used as the working electrode; (ii) a saturated calomel electrode (SCE) was used as the reference electrode; and (iii) a Pt foil was used as the counter electrode. To prepare the working electrode, catalyst ink was first prepared as follows: 10 mg of the catalyst was added to 3 mL of DI water and 1 mL of isopropanol. 100 μL of 5% Nafion® dispersion was then added and the mixture was stirred and sonicated for 2 h. 10 μL of the catalyst ink was dispersed onto the glassy carbon disk electrode using a micropipette. The dispersion was spread across the surface of the disk and was dried in an air stream to yield a thin film of the active material. The active material loading obtained was ~50 μg cm⁻².

The electrolyte solution was purged with nitrogen for 30 min before any measurements were taken. The working electrode was cycled 20 times at a scan rate of 100 mV s⁻¹ between 0 and 1.20 V (vs. RHE) to produce clean and reproducible surfaces. Cyclic voltammograms (CVs) were measured between 0.05 and 1.20 V vs. RHE at 20 mV s⁻¹ and were used to estimate the electrochemically active

surface area (ECSA) of the electrocatalyst. The electrochemical stability of the uncatalyzed and catalyzed support was tested using potential and load cycling protocols designed in industry to mimic start-stop conditions in an operating fuel cell; please see supporting information Fig. S3 for details of these protocols. All potentials are reported versus the reversible hydrogen electrode (RHE) in this paper.

Fuel cell polarization data was measured at 80 °C and 75% relative humidity in a dedicated fuel cell test station (Scribner Associates, Inc., Model 850C). Membrane electrode assemblies (MEAs) were prepared using a Nafion® NRE211 membrane. A baseline MEA was prepared by spray-painting commercial 46% Pt/C TKK catalyst onto both sides of the membrane using an airbrush. MEAs containing the Pt/RuO₂–SiO₂ catalyst were prepared by painting the catalyst ink onto the gas diffusion layer (GDL) surface, followed by hot-pressing the catalyzed GDL onto both sides of the membrane at 60 °C and 100 kPa. Loadings of 0.2 mg_{Pt} cm⁻² at anode and 0.4 mg_{Pt} cm⁻² at cathode were maintained for both sets of MEAs. Catalyst ink and MEA preparation and testing protocols are described in greater detail under supporting information.

3. Results and discussion

3.1. Characterization of the RuO₂–SiO₂ support material

The results of X-ray diffraction (XRD) measurements on all three catalyst supports are shown in Table 1. The wt% presented in the table takes into account only the crystalline phases present in the sample and does not account for amorphous silica. The diffraction peaks obtained (Fig. 1) for the support material RuO₂–SiO₂ (0.5:0.5) could be completely indexed to a tetragonal unit cell. The average crystallite size of this rutile-structure RuO₂ was 130 nm. The presence of SiO₂ gave rise to a broad feature at low angles. The tetragonal lattice parameters *a* and *c* of the rutile-structure RuO₂ agreed well with the Joint Committee on Powder Diffraction Standards (40-1290) diffraction file.

The lattice parameters were slightly larger in the RuO₂–SiO₂ (0.1:0.9) support than in the other two compositions; the variation observed was within the normal range [49] and was not deemed to be significant. The RuO₂ peaks exhibited both size and microstrain broadening. Both crystallite size and microstrain broadening of RuO₂–SiO₂ (0.5:0.5) increased upon incorporation of platinum nanoparticles.

Transmission electron microscopy (TEM) confirmed the presence of both oxide phases in the support. Fig. 2(a) shows that RuO₂ and SiO₂ formed a fairly uniform mixture and the RuO₂ was distributed over the SiO₂ particles. The RuO₂–SiO₂ (0.5:0.5) sample had an electron conductivity of 5.2(±0.4) S cm⁻¹ which was ~8 orders of magnitude greater than the RuO₂–SiO₂ (0.1:0.9) and RuO₂–SiO₂ (0.3:0.7) samples, as shown in Table 2. This indicated that the RuO₂ percolation necessary for adequate electron conductivity was only observed at a RuO₂-loading of well over 30 mol%.

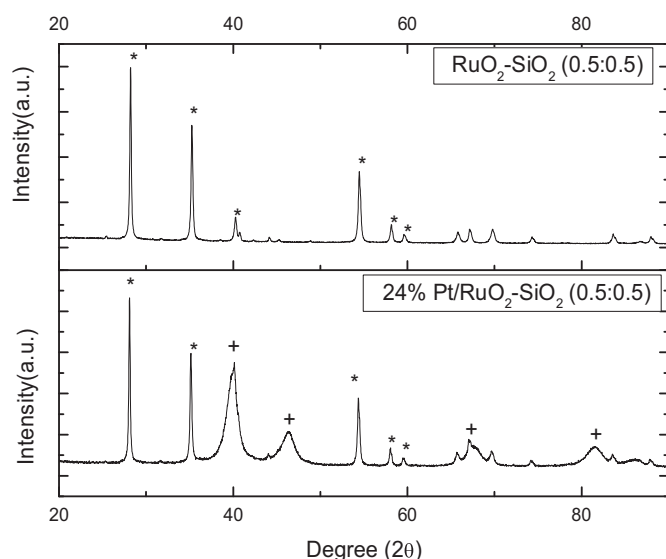


Fig. 1. XRD spectra of RuO₂–SiO₂ support material and Pt/RuO₂–SiO₂ catalyst. *Crystalline RuO₂, + metallic Pt.

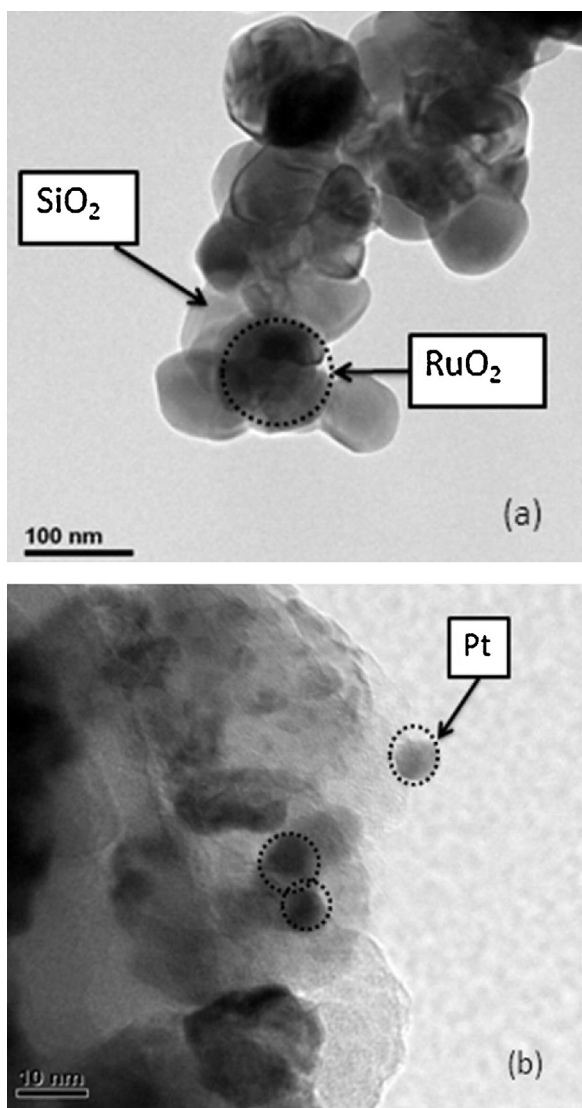


Fig. 2. TEM images of (a) RuO₂-SiO₂ (0.5:0.5) support and (b) 24% Pt/RuO₂-SiO₂ (0.5:0.5).

TEM images of the other compositions (Figs. S4 and S5), confirmed that lower loadings (10 and 30 mol%) of RuO₂ resulted in larger inter-particle separation, and hence a lack of percolation. The results of nitrogen desorption measurements are also shown in Table 2. The BET surface area of the samples decreased with increasing RuO₂ loading. The relatively low surface area RuO₂ particles [50] occluded the pores of the high surface area SiO₂ network [43], causing a decrease in the effective total surface area. Despite this inhibiting effect, the highly conducting RuO₂-SiO₂ (0.5:0.5) material exhibited a BET surface area approaching 300 m² g⁻¹, which was more than adequate for PEFC electrocatalyst support applications and was comparable to the surface area of graphitized carbon [51,52].

Table 2
BET and electrical conductivity.

Support	BET (m ² g ⁻¹)	Conductivity (S cm ⁻¹)
RuO ₂ -SiO ₂ (0.1:0.9)	582 ± 5	3.8 × 10 ⁻⁸
RuO ₂ -SiO ₂ (0.3:0.7)	485 ± 2	8.4 × 10 ⁻⁸
RuO ₂ -SiO ₂ (0.5:0.5)	288 ± 15	5.2 ± 0.4

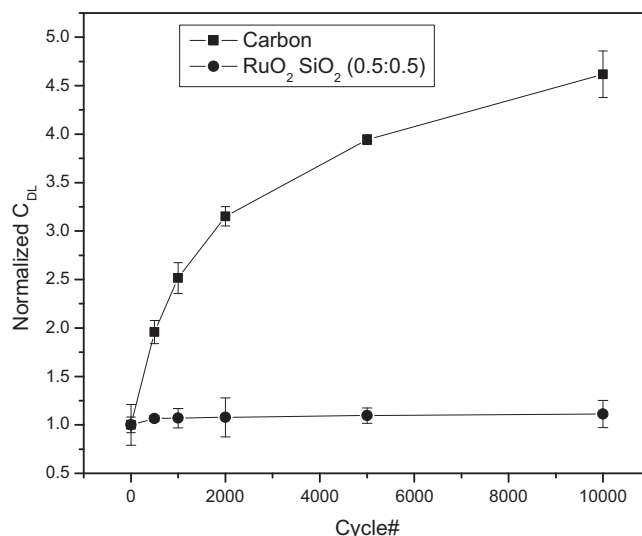


Fig. 3. Normalized double-layer capacitance of carbon and RuO₂-SiO₂ (0.5:0.5) under potential cycling.

3.2. Characterization of Pt/RuO₂-SiO₂

The diffraction pattern of platinum supported on RuO₂-SiO₂ is shown in Fig. 1. The presence of platinum nanoparticles was confirmed by the peak present at $2\theta \approx 40^\circ$ corresponding to the (111) phase of the fcc lattice of platinum. The other three relatively smaller peaks at $2\theta = 47^\circ$, 68° and 81° correspond to the (200), (220) and (311) phases respectively in the fcc lattice of metallic platinum. The crystallite size of platinum, calculated using the Scherrer equation, was found to be 5.8 nm (Table 1). The low intensities and broadening of the peaks was attributed to the small particle size of platinum nanoparticles, as confirmed by TEM (Fig. 2(b)).

The small dark spots represent platinum particles, which are well dispersed and around 5–10 nm in size. The platinum loading on the support was found to be 24 wt% from ICP spectroscopy measurements.

The characterization measurements confirmed that the methods employed yielded a high surface area, electrically conducting uncatalyzed support (RuO₂-SiO₂ (0.5:0.5)) upon which well-dispersed platinum nanoparticles could be deposited at high loadings. Since the other RuO₂-SiO₂ formulations exhibited poor electrical conductivity, the electrochemical stability and fuel cell performance tests were focused on RuO₂-SiO₂ (0.5:0.5) and Pt/RuO₂-SiO₂ (0.5:0.5), as discussed below.

3.3. Electrochemical stability of RuO₂-SiO₂ (0.5:0.5)

The stability of the uncatalyzed support was estimated from the change in double layer capacitance (C_{DL}) at 0.4 V over 10,000 cycles of an accelerated potential cycling test protocol designed to mimic electrode potential transients seen during fuel cell start-up and under fuel starvation conditions. CV was performed at regular intervals during the potential cycling experiment. Fig. S10(a) and S10(b) show representative CVs for the materials tested at the beginning and end of test, and at one intermediate point. The normalized C_{DL} as a function of cycle number for carbon (Vulcan XC-72; baseline material) and RuO₂-SiO₂ (0.5:0.5) are shown in Fig. 3. The carbon baseline exhibited a drastic change (~360%) in the C_{DL}; in contrast, the RuO₂-SiO₂ support only exhibited a 10% change after 10,000 potential cycles. This result suggested that the RuO₂-SiO₂ support was sufficiently durable to withstand even the extreme conditions seen during start-up and shut-down of the PEFC, and during fuel

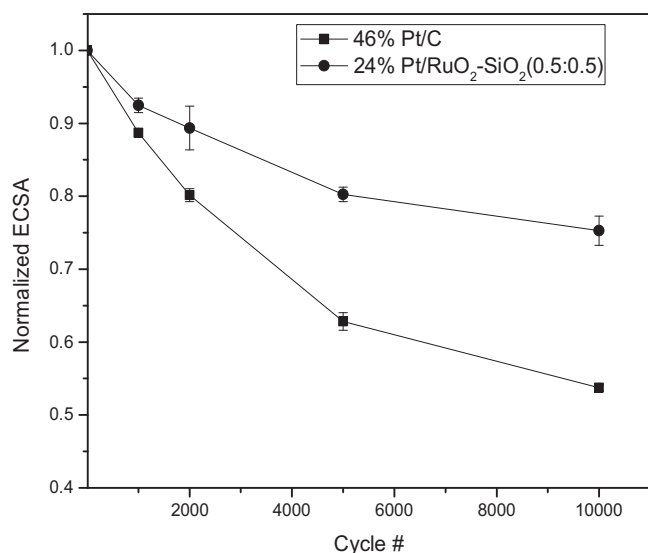


Fig. 4. Normalized ECSA of 46% Pt/C and 24% Pt/RuO₂-SiO₂ (0.5:0.5) under potential cycling as a function of cycle number.

starvation. Both RuO₂ and SiO₂ are known to be stable [53] in acidic environments over a broad potential range, which explains the very modest change in C_{DL} during cycling. The observed change in the C_{DL} of carbon was attributed to the formation of surface groups such as like phenols, lactones and quinones during potential cycling [54].

3.4. Stability of Pt/RuO₂-SiO₂ (0.5:0.5)

The stability of the catalyzed support was estimated from the change in ECSA over 10,000 cycles of an accelerated load cycling test designed to mimic full load-no load transients in an operating PEFC. To calculate the ECSA, the charge corresponding to the desorption of a full monolayer of hydrogen from polycrystalline Pt was assumed to be 210 μC cm⁻². The ECSA of platinum was then calculated using the formula:

$$\text{ECSA} = \left[\frac{Q_{\text{H-adsorption}}}{210 L_{\text{Pt}} \times A_{\text{g}}} \right] 10^5 \quad (2)$$

where $Q_{\text{H-adsorption}}$ was the H₂ adsorption/desorption charge calculated from the CV (Fig. S12(a) and S12(b)), L_{Pt} was the loading of Pt (mg_{Pt} cm⁻²) on the working electrode and A_{g} (cm²) was the geometric area of the working electrode. The response from load cycling tests performed on Pt/C and Pt/RuO₂-SiO₂ electrocatalysts (shown in Fig. 4) revealed that the ECSA of the commercial 46% Pt/C catalyst decreased substantially, with a 46% loss after 10,000 cycles. The Pt/RuO₂-SiO₂ (0.5:0.5) electrocatalyst exhibited a lower, but still significant, ECSA loss of ~33% over 10,000 cycles. Several mechanisms have been identified in literature to explain the reduction in ECSA caused during load cycling [55,56]. In one key mechanism, the platinum particles present are postulated to dissolve (Pt → Pt²⁺ + 2e⁻), migrate, and get re-deposited on other platinum particles, resulting in particle size growth via Ostwald ripening. Previous studies have also reported detection of soluble Pt species during potential cycling in perchloric and sulfuric acid [57]. It has been shown that at potentials below 1 V, the presence of adsorbed oxygen species on Pt (Pt-OH) leads to carbon support corrosion [58].

Pt agglomeration caused by support corrosion can also cause the decrease in ECSA seen in Fig. 4. Realistically, the latter mode of ECSA loss is the only mode that can be mitigated by using a corrosion resistant support. The results obtained suggest that loss in ECSA during load cycling was modestly lowered by using a corrosion resistant support. This conclusion must be tempered

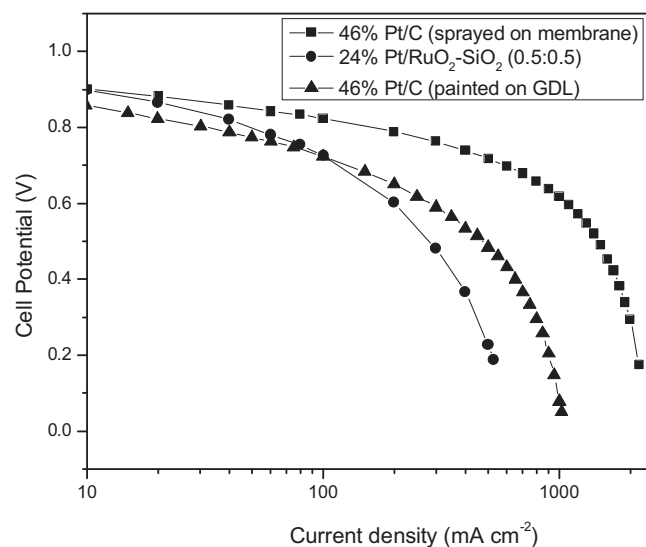


Fig. 5. Polarization curves for 46% Pt/C commercial TKK catalysts and 24% Pt/RuO₂-SiO₂ (0.5:0.5) in H₂/air. MEA preparation by spraying ink on membrane for Pt/C catalyst and by hand painting ink on GDL for both 46% Pt/C and 24% Pt/RuO₂-SiO₂ (0.5:0.5).

with the knowledge that the Pt/RuO₂-SiO₂ (0.5:0.5) sample contained 6 nm diameter platinum nanoparticles. The lower surface free energy of these relatively larger nanoparticles (compared to the 3 nm average diameter particles in the Pt/C baseline) would also lead to lower rates of platinum dissolution and hence lower ECSA loss.

3.5. Fuel cell performance of 24% Pt/RuO₂-SiO₂ (0.5:0.5)

Electrochemical impedance spectroscopy was performed to independently estimate the ion transport resistance in the electrolyte and the electrode. The Nyquist plots obtained on MEAs prepared with 46% Pt/C and 24% Pt/RuO₂-SiO₂ (0.5:0.5) operated in H₂/N₂ mode at 80 °C and 75% RH are shown in Fig. S17. At high frequencies, a 45° line incident onto the real axis was observed, in line with expectations [59]. Please see supplementary information for a detailed explanation of resistance calculations. The ion transport resistance in the electrode (R_{elec}) and electrolyte ($R_{\text{m+c}}$), of which the latter includes contact resistances [59], for the MEA prepared with 46% Pt/C was found to be 0.18 Ω cm² and 0.15 Ω cm² respectively. The corresponding values for the MEA prepared with 24% Pt/RuO₂-SiO₂ (0.5:0.5) were found to be 0.24 Ω cm² and 0.13 Ω cm² respectively. The electrolyte resistance was nearly identical for both MEAs, a reasonable observation given that the MEAs both contained the same electrolyte. The observed trend in electrode resistance is further discussed below.

Polarization curves were obtained on MEAs prepared with 46% Pt/C baseline and 24% Pt/RuO₂-SiO₂ electrocatalysts with hydrogen as fuel and various oxidants (see Figs. 5 and S16, and supporting information for details). MEAs prepared by coating catalyst ink onto the GDL had a lower fuel cell performance than MEAs with the catalyst sprayed onto the membrane. The spray painting of 24% Pt/RuO₂-SiO₂ on the membrane was attempted several times, but did not yield very good results due to the higher density of the catalyst powder.

The performance of the Pt/RuO₂-SiO₂ catalyst is plotted along with two benchmark Pt/C performance curves obtained using two MEAs, one prepared by spraying catalyst ink onto the membrane and the second by painting it onto the GDL. For data analysis, the performance was evaluated against the best performing benchmark which was 46% Pt/C ink sprayed on membrane.

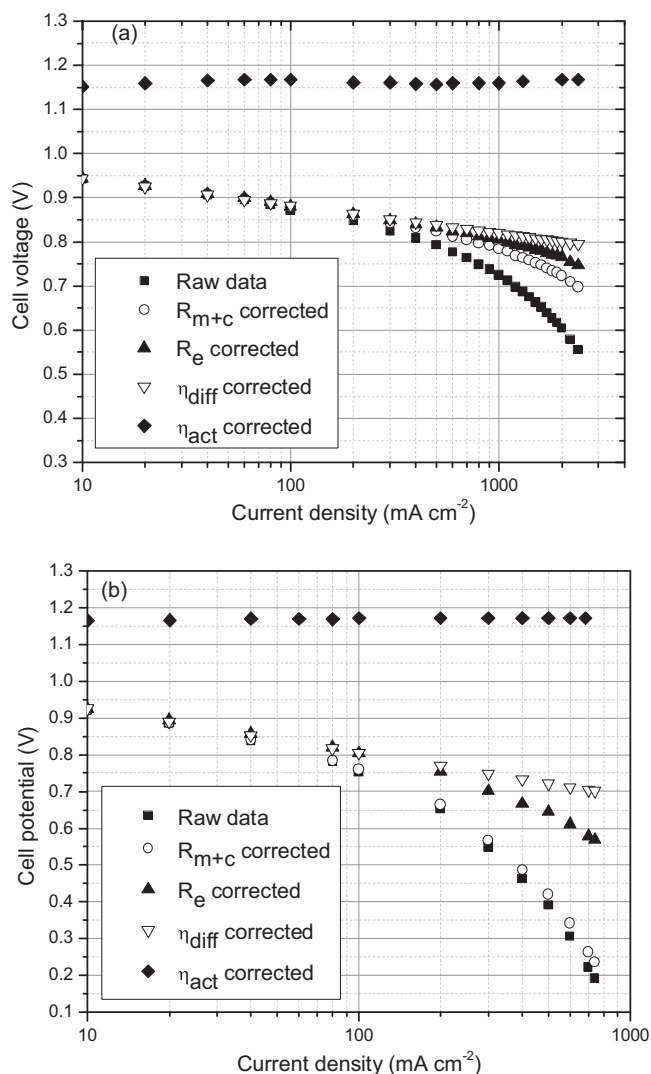


Fig. 6. Polarization curves of (a) 46% Pt/C and (b) 24% Pt/RuO₂-SiO₂ (0.5:0.5) at 80 °C and 75% RH with oxygen as the oxidant.

The polarization curves were analyzed using a method described in detail in the literature [60] to deconvolute the contribution of individual polarization sources to the overall cell overpotential. The results of this analysis using oxygen and air as the oxidants are shown in Figs. 6 and S18 and tabulated (at a current density of 500 mA cm⁻²) in Table S1. Briefly, the procedure followed for any given MEA was as follows: first, using the value for R_{m+c} obtained from impedance spectroscopy (Fig. S17), the raw data obtained was corrected for electrolyte and contact resistance to obtain iR_{free} data. Second, the electrode resistance, R_e was estimated using the current-ratio method [60], wherein guessed estimates of R_e were successively used to correct the data until arriving at the value for R_e that yielded current ratios at a fixed overpotential that was equal to ratios of the corresponding oxygen concentrations at the cathode inlet. R_{elec} values from impedance spectroscopy did not reflect correct electrode resistance values since non-ideal capacitive behavior was observed at low frequencies, likely due to H₂ crossover and oxidation at the cathode. The R_e in the 24% Pt/RuO₂-SiO₂ (0.5:0.5) based electrode was higher (0.5 Ω cm² compared to 0.02 Ω cm² for 46% Pt/C) due to the relatively lower conductivity of the catalyst support vs. carbon and the high volume percent of binder used, which isolated the support particles. A higher platinum loading and an optimized binder/support ratio will overcome this barrier.

Third, diffusion limitations in zones wherein there was no chemical reaction (GDL, binder film surrounding electrocatalyst particles) were accounted for by plotting overpotential vs. $i/(1 - i/i_{lim})$ where i_{lim} is the limiting current value for a given oxidant. A plot of $\log(i/(1 - i/i_{lim}))$ vs. iR_{free} cell voltage yielded a straight line for the correct value of i_{lim} , which was estimated through iteration as described in Ref. [57]. Limiting currents for 46% Pt/C and 24% Pt/RuO₂-SiO₂ (0.5:0.5) in H₂/air mode were found to be 1080 and 560 mA cm⁻² respectively. The higher mass transfer limitation in the MEA with 24% Pt/RuO₂-SiO₂ (0.5:0.5) catalyst was attributed to the higher volume percent loading of Nafion® binder within the electrode, which arose due to the higher density of RuO₂-SiO₂ (0.5:0.5) compared to carbon.

This resulted, on average, in thicker ionomer films around the electrocatalyst particles, presenting a larger diffusion resistance to oxygen transport. An ideal binder/support ratio needs to be maintained to ensure facile mass transport in the electrodes; optimization of this ratio was outside of the scope of this paper.

To study whether the oxygen diffusion losses in these catalysts were due to condensed phase diffusion (binder, liquid water) or gas phase diffusion (pore diffusion) limitations, the polarization data obtained with air, oxygen and helox as oxidants was analyzed. The helox-air (21% O₂/He-21% O₂/N₂) gain was defined as the difference in cell voltage at a given current density when helox and air were used as oxidants. Oxygen has better diffusivity in helox than in air due to the smaller size of helium relative to nitrogen [61]. The helox-air gain would be considerable if the transport of oxidants in the cathode were subject to gas phase diffusion limitations. However, if diffusion in condensed phases like water and binder films were limiting oxidant transport, the resultant helox-air gain would be negligible.

The oxygen-air gain was defined as the difference in cell voltage at a given current density when oxygen and air were used as the oxidant. Theoretically, the oxygen-air gain should be 49 mV at 80 °C assuming a Tafel slope of 70 mV/dec [62]. Deviation of the oxygen-air gain from this value is indicative of mass transport limitations within the electrode. A plot of helox-air gain vs. oxygen-air gain would result in all points clustering around (50, 0) if there were no mass transfer losses. The extent of deviation from this point indicates the magnitude of the overpotential due to mass transfer limitations; the slope of the trend line provides insights into whether gas phase or condensed phase limitations dominate the mass transport overpotential. A slope value of zero would represent total binder phase diffusion limitations.

To summarize, by plotting the oxygen-air gain vs. the helox-air gain, one can determine: (a) whether mass transport limitations exist within the electrode; and (b) whether gas-phase or condensed-phase limitations dominate losses due to mass transport. The plots of helox-air gain vs. oxygen-air gain for MEAs prepared with 46% Pt/C and 24% Pt/RuO₂-SiO₂ (0.5:0.5) are shown in Fig. 7. The trend for 46% Pt/C showed several points lying around (50, 0), with a slope of 0.42 for points deviating from this value. The slope suggested that there were significant gas phase limitations in the electrode; however these limitations were present only for current densities greater than 500 mA cm⁻². The corresponding trend for 24% Pt/RuO₂-SiO₂ (0.5:0.5) showed very few points clustering around (50, 0), with a slope of 0.82 for points deviating from this value. The slope again suggested significant gas phase diffusion limitations. The key difference between the 2 MEAs was in the magnitude of the mass transport limitations. Points on the gain plot were found to be further away from (50, 0) even at low current densities in MEAs containing the non-carbon catalyst support. At a current density of 200 mA cm⁻², the MEA prepared with 24% Pt/RuO₂-SiO₂ (0.5:0.5) displayed an oxygen-air gain of ~120 mV and a helox-air gain of ~75 mV. The corresponding point

Table 3
Comparison of activities in the MEA.

Sample	Loading, A/C (mg cm ⁻²)	ECSA (m ² g ⁻¹)	Mass-specific activity, $I_{m(0.9V)}$ (A mg _{Pt} ⁻¹)	Area-specific activity, $I_{s(0.9V)}$ (μA cm _{Pt} ⁻²)
46% Pt/C	0.2/0.4	76 ± 4	0.150	198
24% Pt/RuO ₂ -SiO ₂ (0.5:0.5)	0.2/0.4	32 ± 2	0.050	156

for the MEA prepared with 46% Pt/C was around (50, 0) which implied that the combined mass transport losses were much more significant for the non-carbon based catalyst even at low current densities. The transport limitations within the electrocatalyst layer were attributed to the non-optimal binder/support ratio in the MEA prepared with 24% Pt/RuO₂-SiO₂ (0.5:0.5). Further discussion as to the reasons for higher mass transport and ohmic losses in the MEA prepared with 24% Pt/RuO₂-SiO₂ (0.5:0.5) are presented under supplementary information.

The Tafel slope, mass activity, and area specific activity were calculated from the straight line (activation controlled line) obtained after accounting for ohmic and transport losses within the MEA. Tafel slopes for 46% Pt/C and 24% Pt/RuO₂-SiO₂ (0.5:0.5) were found to be 62 mV/dec and 116 mV/dec respectively. The 'double Tafel' obtained in the latter case suggested there were considerable transport limitations within the electrocatalyst layer itself, in regions where a mixed reaction and diffusion regime existed [63]. Note that the earlier correction only accounted for mass transport losses in regions where diffusion occurred in the absence of reaction (i.e. in the GDL, and within the Nafion® binder film encapsulating catalyst particles).

The current density at an overpotential of 275 mV (or equivalently 0.9 V vs. RHE) was used as a metric to establish a quantitative comparison of catalyst activity. At this overpotential, the current densities were sufficiently high to neglect effects of mixed potential and hydrogen crossover, but also sufficiently low for concentration polarization and ohmic polarization to be small. The current densities observed in MEAs prepared with 46% Pt/C and 24% Pt/RuO₂-SiO₂ (0.5:0.5) were found to be 60 and 20 mA cm⁻² respectively. The mass activity was calculated by normalizing this current density by the loading of Pt; area-specific activity was calculated by normalizing the current density with the measured ECSA.

The 24% Pt/RuO₂-SiO₂ (0.5:0.5) catalyst had lower mass and area-specific activities when compared to the baseline 46% Pt/C

catalyst, as shown in Table 3. The reported activities of the baseline 46% Pt/C were consistent with those available in the literature [64]. The catalytic activity depends considerably on the platinum particle size and morphology. While the specific activity is nearly independent of [63], and perhaps even increases with crystallite size (crystallite size effect), the lower availability of surface platinum atoms due to poor dispersion leads to poor mass activity in larger crystallites. Pt/C, having smaller platinum particles (~2.8 nm [64]), demonstrated superior activity and turnover compared to Pt/RuO₂-SiO₂ (0.5:0.5) and therefore exhibited lower activation losses. The lower mass activity of the 24% Pt/RuO₂-SiO₂ (0.5:0.5) was attributed to the larger particle size of platinum as evidenced by the XRD and TEM results (Figs. 1 and 2). The larger platinum particle size on the RuO₂-SiO₂ support also resulted in lower exposed platinum surface and consequently to lower value of ECSA, as reported in Table 3.

4. Conclusions

A novel mixed oxide catalyst support was investigated for use in PEFC electrocatalysts. A high-surface area porous SiO₂ matrix was doped with electrically conducting RuO₂. Three different formulations of RuO₂:SiO₂ with molar ratios of 01:0.9, 0.3:0.7 and 0.5:0.5 were synthesized and tested. RuO₂ and SiO₂ in the 0.5:0.5 molar ratio was shown to have a high BET surface area of ~290 m² g⁻¹ as well as an excellent electrical conductivity of 5 S cm⁻¹. This material displayed remarkably high electrochemical stability, wherein the change in double layer capacitance was only 10% (compared to 360% for carbon) after aggressive accelerated potential cycling tests. Pt deposition onto this support was carried out via a conventional impregnation–reduction method using NaBH₄ as a reducing agent. The resultant catalyst (24 wt% Pt loading) was more stable than the commercial Pt/C baseline, with a loss of ECSA of ~33% compared to ~46% for Pt/C after 10,000 load cycles. Although more stable, the 24% Pt/RuO₂-SiO₂ catalyst had lower activity in an operating fuel cell compared with the commercial Pt/C. Fuel cell polarization curves were analyzed to decipher the relative contributions of the various losses occurring during fuel cell operation. There were larger losses due to electrode ohmic resistance in MEAs prepared with the 24% Pt/RuO₂-SiO₂ catalysts. This was attributed to lower support conductivity vs. carbon and to a higher volume fraction of binder in the electrode. Mass transport losses were also considerably higher due to the excess volume percent of binder within electrodes prepared using this catalyst. The mass and specific activities observed in the 24% Pt/RuO₂-SiO₂ catalysts were limited mainly by the platinum particle size. Future work will focus on (1) controlling the size and morphology of platinum particles to achieve lower particle size, preferably to 2–4 nm, as found in commercial state-of-the-art Pt/C catalysts [64]; and (2) optimizing the binder/support ratio to yield high performance electrodes.

Acknowledgments

The authors would like to acknowledge Prof. James Kaduk, Department of Biological and Chemical Sciences, Illinois Institute of Technology for powder X-ray diffractograms and Rietveld analyses. This work was supported by NSF Award # 0847030.

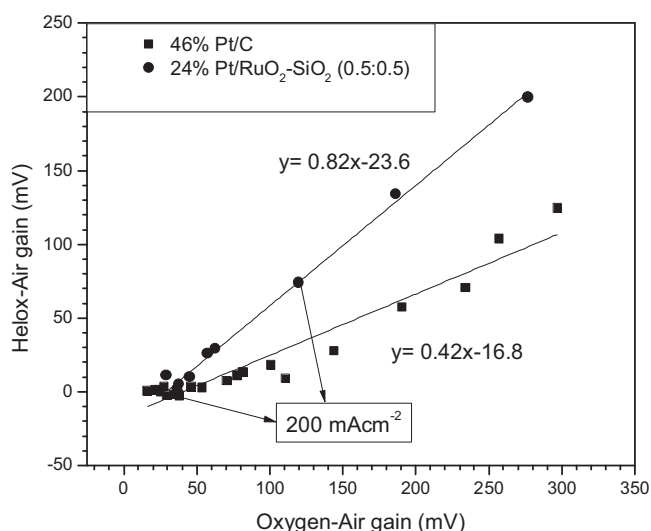


Fig. 7. Plot of helox-air gain vs. oxygen-air gain for 46% Pt/C and 24% Pt/RuO₂-SiO₂ (0.5:0.5).

Appendix A. Supplementary data

Supplementary data associated with this article can be found, in the online version, at <http://dx.doi.org/10.1016/j.apcatb.2013.02.015>.

References

- [1] R. Borup, J. Meyers, B. Pivovar, Y.S. Kim, R. Mukundan, N. Garland, D. Myers, M. Wilson, F. Garzon, D. Wood, P. Zelenay, K. More, K. Stroh, T. Zawodzinski, J. Boncella, J.E. McGrath, M. Inaba, K. Miyatake, M. Hori, K. Ota, Z. Ogumi, S. Miyata, A. Nishikata, Z. Siroma, Y. Uchimoto, K. Yasuda, K.-I. Kimijima, N. Iwashita, *Chemical Reviews* 107 (2007) 3904–3951.
- [2] K. Kinoshita, J.A.S. Bett, *Carbon* 11 (1975) 403.
- [3] A.A. Franco, M. Guinard, B. Barthe, O. Lemaire, *Electrochimica Acta* 54 (2009) 5267.
- [4] P.T. Yu, W. Gu, J. Zhang, R. Makharia, F.T. Wagner, H.A. Gasteiger, F.N. Büchi, M. Inaba, T.J. Schmidt, *Polymer Electrolyte Fuel Cell Durability*, Springer, New York, NY, 2009, 29–53.
- [5] T.J. Schmidt, H.A. Gasteiger, G.D. Stab, P.M. Urban, D.M. Kolb, R.J. Beh, *Journal of the Electrochemical Society* 145 (1998) 2354.
- [6] E. Antolini, *Applied Catalysis B* 88 (2009) 1.
- [7] M. Min, J. Cho, K. Cho, H. Kim, *Electrochimica Acta* 45 (2000) 4211.
- [8] Y.-J. Wang, D.P. Wilkinson, J. Zhang, *Chemical Reviews* 111 (2011) 7625–7651.
- [9] S.T. Oyama, *Chemistry of Transition Metal Carbides and Nitrides*, 1st ed, Springer, 1996.
- [10] S.A.G. Evans, J.G. Terry, N. Plank, A. Walton, L. Keane, C. Campbell, P. Ghazal, J. Beattie, T. Su, J. Crain, A. Mount, *Electrochemistry Communications* 7 (2005) 125.
- [11] O.T. Musthafa, S. Sampath, *Chemical Communications* (2008) 67.
- [12] B. Avsarala, P. Halder, *Electrochimica Acta* 55 (2010) 9024–9034.
- [13] N. Liu, K. Kourtakis, J.C. Figueroa, J.G. Chen, *Journal of Catalysis* 215 (2003) 254.
- [14] H. Chhina, S. Campbell, O. Kesler, *Journal of Power Sources* 164 (2007) 431.
- [15] M.B. Zellner, J.G. Chen, *Catalysis Today* 99 (2005) 299.
- [16] R. Ganesan, D.J. Ham, J.S. Lee, *Electrochemistry Communications* 9 (2007) 2576.
- [17] Y. Hara, N. Minami, H. Matsumoto, H. Itagaki, *Applied Catalysis A* 332 (2007) 289.
- [18] Y. Hara, N. Minami, H. Itagaki, *Applied Catalysis A* 323 (2007) 86.
- [19] K. Kolbrecka, J. Przyłski, *Electrochimica Acta* 39 (1994) 1591.
- [20] G. Chen, S.R. Bare, T.E. Mallouk, *Journal of the Electrochemical Society* 149 (2003) A1092.
- [21] T. Ioroi, Z. Siroma, N. Fujiwara, S. Yamazaki, K. Yasuda, *Electrochemistry Communications* 7 (2005) 183.
- [22] T. Ioroi, T. Akita, S.-I. Yamazaki, Z. Siroma, N. Fujiwara, K. Yasuda, *Journal of the Electrochemical Society* 158 (2011) C329–C334.
- [23] S.Y. Huang, P. Ganesan, S. Park, B.N. Popov, *Journal of the American Chemical Society* 131 (2009) 13898.
- [24] K.W. Par, K.S. Seol, *Electrochemistry Communications* 9 (2007) 2256.
- [25] C.V. Subban, Q. Zhou, A. Hu, T.E. Moylan, F.T. Wagner, F.J. DiSalvo, *Journal of the American Chemical Society* 132 (2010) 17531–17536.
- [26] O.E. Haas, S.T. Briskeby, O.E. Kongstein, M. Tsyppkin, R. Tunold, B.T. Børresen, *Journal of New Materials for Electrochemical Systems* 11 (2008) 9.
- [27] A. Wang, H. Xu, Y. Lu, J. Hu, X. Kong, B. Tian, H. Dong, *Chinese Journal of Catalysis* 30 (2008) 179.
- [28] M.S. Saha, R. Li, M. Cai, X. Sun, *Electrochemical and Solid-State Letters* 10 (2007) B130.
- [29] K.Y. Chen, A.C.C. Tseung, *Journal of the Electrochemical Society* 143 (1996) 2703.
- [30] V. Raghuvveer, B. Viswanathan, *Journal of Power Sources* 144 (2005) 1.
- [31] T. Maiyalagan, B. Viswanathan, *Journal of Power Sources* 175 (2008) 789.
- [32] Y. Suzuki, A. Ishihara, S. Mitsuhashi, N. Kamiya, K. Ota, *Electrochemical and Solid-State Letters* 10 (2007) B105.
- [33] Y. Zhang, H. Zhang, Y. Zhai, X. Zhu, C. Bi, *Journal of Power Sources* 168 (2007) 323.
- [34] H. Chhina, S. Campbell, O. Kesler, *Journal of Power Sources* 161 (2006) 893.
- [35] I. Eswaramoorthi, A.K. Dalai, *International Journal of Hydrogen Energy* 34 (2009) 2580.
- [36] Y. Feng, R. Yao, L. Zhang, *Physica B* 350 (2004) 348.
- [37] H. Wakayama, N. Setoyama, Y. Fukushima, *Advanced Materials* 15 (2003) 742–745.
- [38] J.P. Zheng, T.R. Jow, *Journal of the Electrochemical Society* 142 (1995) L6–L8.
- [39] C.N. Chervin, A.M. Lubers, J.W. Long, D.R. Rolison, *Journal of Electroanalytical Chemistry* 644 (2010) 155–163.
- [40] H. Ma, C. Liu, J. Liao, Y. Su, X. Xue, W. Xing, *Journal of Molecular Catalysis A: Chemical* 247 (2006) 7–13.
- [41] M. Watanabe, S. Motoo, *Journal of Electroanalytical Chemistry* 60 (1975) 267.
- [42] H.A. Gasteiger, N. Markovic, P.N. Ross, E. Cairns, *Electrochimica Acta* 39 (1994) 1825.
- [43] J.-H. Smätt, S. Schunk, M. Lindén, *Chemistry of Materials* 15 (2003) 2354–2361.
- [44] Y. Lin, X. Cui, C.H. Yen, C.M. Wai, *Langmuir* 21 (2005) 11474–11479.
- [45] S. Musić, S. Popović, M. Maljković, K. Furić, A. Gajović, *Journal of Materials Science Letters* 21 (2002) 1131–1134.
- [46] C.I. Merzbacher, J.G. Barker, J.W. Long, D.R. Rolison, *Nanostructured Materials* 12 (1999) 551–554.
- [47] J.W. Guo, T.S. Zhao, J. Prabhuram, C.W. Wong, *Electrochimica Acta* 50 (2005) 1973–1983.
- [48] B.H. Toby, *Journal of Applied Crystallography* 34 (2001) 210–213.
- [49] S. Bhaskar, P.S. Dobal, S.B. Majumder, R.S. Katiyar, *Journal of Applied Physics* 89 (2001) 2987–2992.
- [50] D. Rochefort, D. Guay, *Journal of Alloys and Compounds* 400 (2005) 257–264.
- [51] M. Uchida, Y. Fukuoka, Y. Sugawara, N. Eda, A. Ohta, *Journal of the Electrochemical Society* 143 (1996) 2245–2252.
- [52] J.J. Niu, J.N. Wang, *Electrochimica Acta* 53 (2008) 8058–8063.
- [53] D.R. Rolison, B. Dunn, *Journal of Materials Chemistry* 11 (2001) 963–980.
- [54] K. Kinoshita, *Carbon: Electrochemical and Physicochemical Properties*, Wiley, New York, 1988.
- [55] P.J. Ferreira, G.J. La O, Y. Shao-Horn, D. Morgan, R. Makharia, S. Kocha, H.A. Gasteiger, *Journal of the Electrochemical Society* 152 (2005) A2256.
- [56] E. Antolini, *Journal of Materials Science* 38 (2003) 2995.
- [57] D.C. Johnson, D.T. Napp, S. Bruckenstein, *Electrochimica Acta* 15 (1970) 1493.
- [58] B. Merzougui, S. Swathirajan, *Journal of the Electrochemical Society* 153 (2006) A2220–A2226.
- [59] R. Makharia, M.F. Mathias, D.R. Baker, *Journal of the Electrochemical Society* 152 (2005) A970–A977.
- [60] M.V. Williams, H.R. Kunz, J.M. Fenton, *Journal of the Electrochemical Society* 152 (2005) A635–A644.
- [61] Y.W. Rho, O.A. Velev, S. Srinivasan, Y.T. Kho, *Journal of the Electrochemical Society* 141 (1994) 2084–2089.
- [62] S. Sambandam, V. Ramani, *Physical Chemistry Chemical Physics* 12 (2010) 6140–6149.
- [63] H.R. Kunz, G.A. Gruver, *Journal of the Electrochemical Society* 122 (1975) 1279–1287.
- [64] H.A. Gasteiger, S. Kocha, B. Sompalli, F.T. Wagner, *Applied Catalysis B* 56 (2005) 9.